On the road to metallic nanoparticles by rational design: bridging the gap between atomic-level theoretical modeling and reality by total scattering experiments

B. K. Prasai[1], A. R. Wilson[2], B. J. Wiley[2], Y. Ren[3], V. Petkov[1,*]

Department of Physics, Central Michigan University, Mt. Pleasant, MI 48858, USA

[2]Department of Chemistry, Duke University, Durham, NC 27708, USA

[3]Advanced Photon Source, Argonne National Laboratory, Argonne, IL 60439, USA

COMPUTATIONAL METHODS AND EXPERIMENTAL DATA

Classical Molecular Dynamics (MD) Simulations

MD simulations were carried out with the help of computer program DL-POLY [S1] under canonical NVT ensemble in the absence of periodic boundary conditions. Velocity Verlet algorithm with a time step of 2 fs was used. Since, in general, the realism of a classical MD simulation is dependent on the model chosen considering the conditions under which the simulation is run the initial atomic configurations for Au-Pd, pure Au and Fe-Pd NPs studied here reflected their actual size, shape, chemical composition and pattern as determined by TEM, HR-TEM, HAADF-STEM, ICP-AES and EDS experiments described in the text. The initial atomic configurations were annealed at 700 K for 200 ps. Note, 700 K is about the maximum temperature at which any of NPs studied here have been synthesized and/or post-synthesis treated (see Experimental section in the text). Also, 700 K is well above the temperature at which any of NPs studied here are meant to be used (see Introduction and Experimental section in the text). The configurations were then cooled down to room temperature (300 K) in steps of 50 K in 1200 ps and equilibrated at that temperature for another 100 ps. Thus MD generated NP structure models and room-temperature obtained atomic PDF data, against which the models and their theoretical foundation were tested and refined, were put on the same thermodynamic footing.

Reverse Monte Carlo Simulations

Reverse Monte Carlo (RMC) simulations were used to refine further MD structure models for fully activated Au-Pd alloy NPs, shown in Figure 6(left), and $Fe_{48}Pd_{52}$ alloy NPs, shown in Figure 9(right). In the spirit of traditional RMC simulations [S2, S3] the positions of atoms in the MD models were adjusted as to minimize the difference between the model-computed and respective experimental atomic PDFs. During the simulations atoms were constrained to maintain as maximal (i.e. as close to 12) as possible coordination numbers thus taking into account the close packed nature (see text) of the atomic arrangement in NPs listed above. Also, atoms were constrained not to come closer than pre-selected distances of closest approach thus

taking into account the fact that metallic species may not approach each other much closer than the sum of their radii R_{ij}. Atomic radii used in the RMC simulations were determined from the positions of the first peak in the partial atomic PDFs computed from the respective MD models. A relatively new feature [S4, S5] turning the simulations into a hybrid between traditional RMC and MD, was the optimization of model's energy. The simultaneous minimization of model's energy and the difference between model-computed and experimental PDF data is important since if the former or latter are done alone some inherent to NPs structural features (e.g. local structural disorder) may end up under or overestimated, respectively. Model's energy was described by a pair-wise (Lennard-Jones type) potentials the parameters of which were taken from literature sources [S6]. The simulations were considered completed when no significant changes in the goodness-of fit indicator R_{wp} described below were observed. Simulations were done with the help of a new version of the program RMC++ [S7]. Note hybrid RMC described here is very much different from the so-called Empirical Potential Structure Refinement (EPSR) simulations which feature somewhat disordered but continuous atomic configurations subjected to 3D periodic boundary conditions [S8, S9].

Evaluation the quality of structure models for metallic NPs studied here

The quality of structure models built by MD and that of the models refined by hybrid RMC was evaluated by computing a goodness-of-fit indicator R_{wp} , defined as [S10- S12]:

$$R_{wp} = \left\{ \frac{\sum w_i (G_i^{\exp.} - G_i^{calc.})^2}{\sum w_i (G_i^{\exp.})^2} \right\}^{1/2} \quad (1)$$

where $G^{exp.}$ and $G^{calc.}$ are the experimental and model computed atomic PDFs, respectively, and w_i are weighting factors reflecting the experimental uncertainty of the individual $G^{exp.}$ data points. Here w_i were considered to be uniform which, as predicted by theory [S12] and largely corroborated by experiment [S13], is a reasonable approximation in the case of high quality $G^{exp.}$ data such as ours. Note R_{wp} is conceptually very similar to the weighted profile agreement factor R_{wp}^{Bragg} [S14, S15] used for evaluating how well a crystal structure model reproduces experimental powder diffraction data defined as:

$$R_{wp}^{Bragg} = \left\{ \frac{\sum w_i (y_i^{\exp.} - y_i^{calc.})^2}{\sum w_i (y_i^{\exp.})^2} \right\}^{1/2} \quad (2)$$

where y_i^{exp} and y_i^{calc} are, respectively, the observed and model calculated intensities at the step i in the polycrystalline powder diffraction pattern, and w_i are weighting factors reflecting the quality of experimental powder diffraction data. The typical values of R_{wp} for high-quality NP structure models are, however, in the range of 15-25 % (see text) that appears somewhat high when compared to that of R_{wp}^{Bragg} values (usually less than 10 %) [S14, S15]. This mostly reflects the fact that total scattering experiments on NPs and, hence, atomic PDFs derived from the experiments take both Bragg-like features and the usually strong diffuse component (e.g. see Figure S5 below) of the experimental diffraction patterns into account while crystal structure determination from powder diffraction data focuses on sharp Bragg peaks alone. The inherently

higher absolute values of the goodness-of-fit indicator R_{wp} , however, do not affect its functional purpose as a quantity allowing evaluating the quality of NP structure models unambiguously.

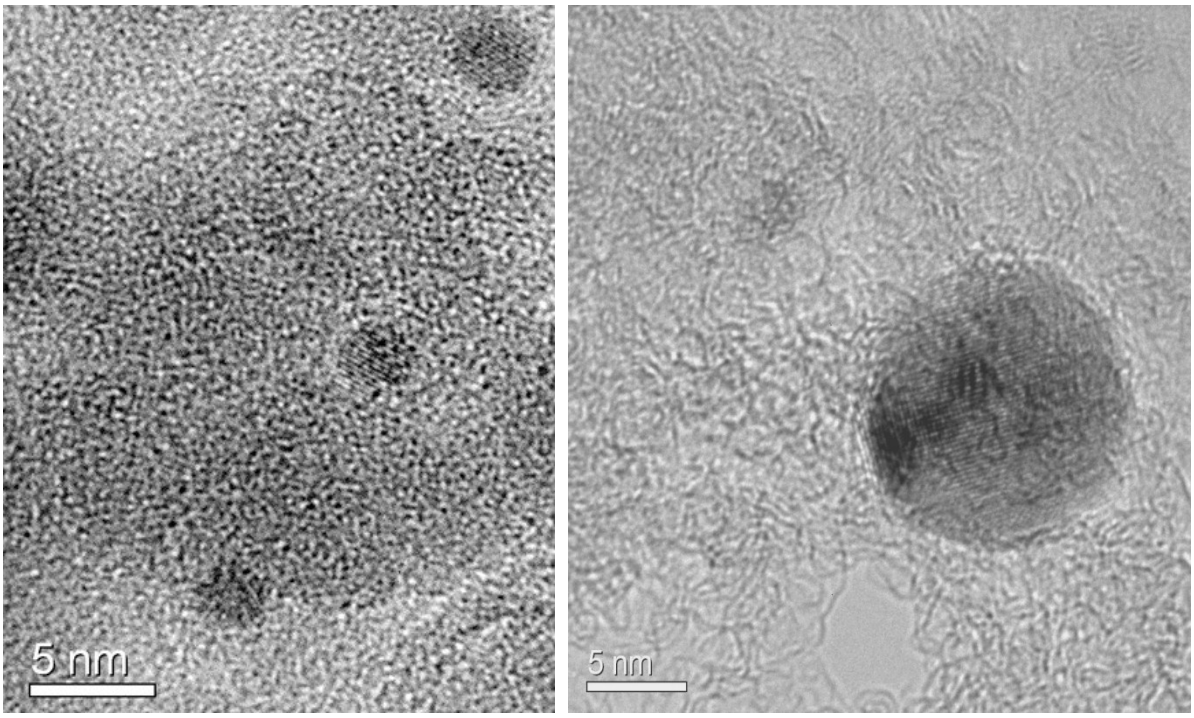

Figure S1. *(left)* Representative high-resolution TEM image of silica supported Au seeds used for producing Au core-Pd shell NPs. Seeds appear with an average size of approximately 4.1(± 0.5) nm. Note the "±" deviation from the average size of Au seeds reported here is half width at full maximum of gaussian-like distribution of sizes extracted from a population of about 300-400 different Au seeds appearing on different TEM images. (*right)* Representative high-resolution image of ~ 15 nm in size Au particle. Earlier TEM experiments [41] on Au NPs studied here found that their size is approximately 15(± 1.5) nm. TEM image of Au NP shown above (right) confirms the findings of those studies. Note, lattice fringes are seen inside the Au seeds and Au nanoparticle indicating a good overall degree of crystallinity. Fringes, however, disappear near the surface of Au seeds and Au nanoparticle indicating that both suffer substantial atomic positional disorder, in particular close to the seed/NP surface.

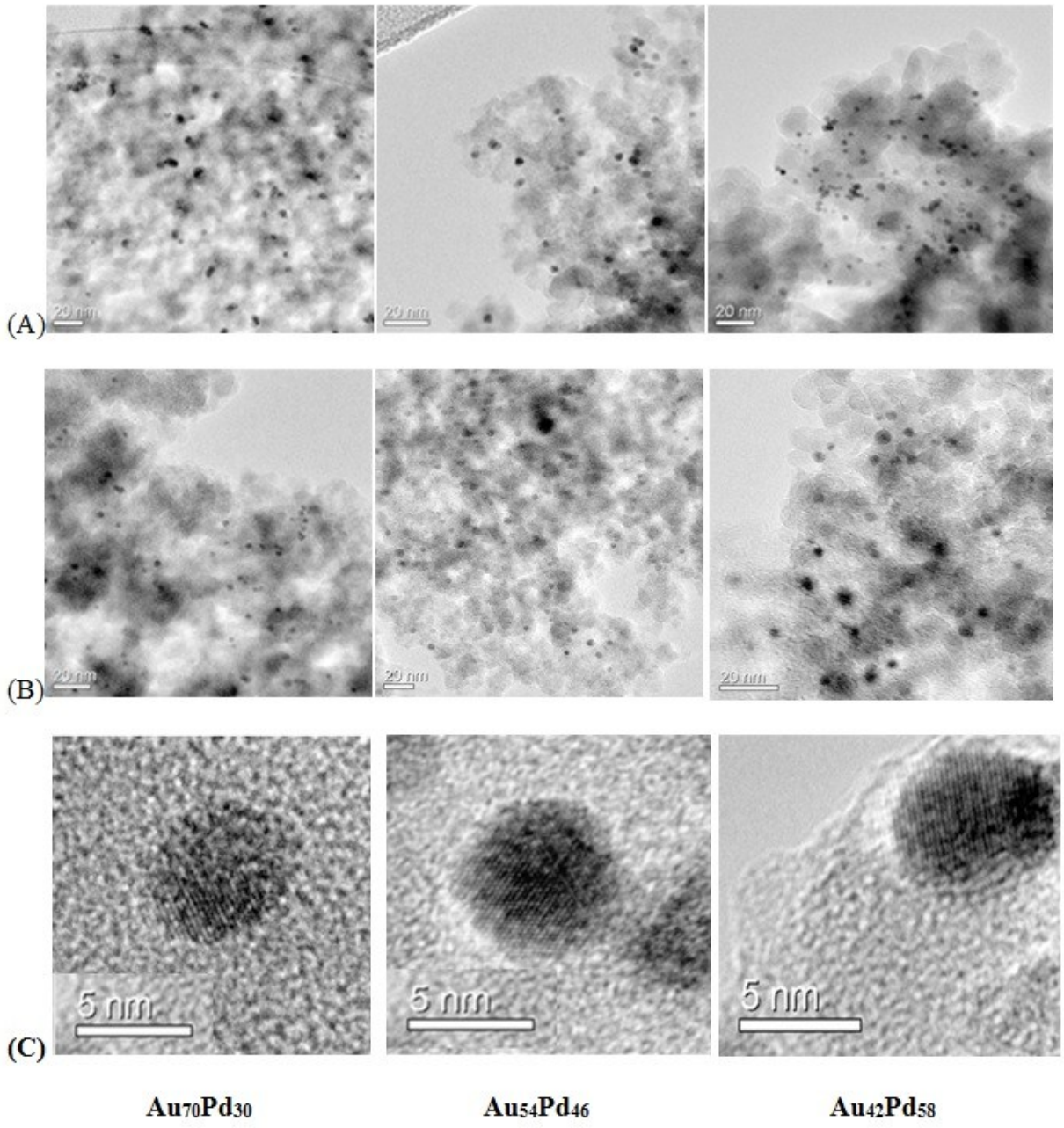

Figure S2. Representative TEM (A) and (B), and high-resolution TEM (C) images of silica supported $Au_{100-x}Pd_x$ particles (x=30, left column); (x=46, middle column) and (x=58; right column). First row (A) shows fresh NPs, second row (B) – fully activated NPs and third row (C) – selected fully activated NPs. NPs appear with an average size of approximately 4.5, 5.0 and 5.5 (± 0.9) nm for x = 30, 46 and 58, respectively. Note the "±" deviation from the average NP size reported here is half width at full maximum of gaussian-like distribution of sizes extracted from populations of 400 to 500 different NPs appearing on different TEM images. HR-TEM images (C) show lattice fringes inside the NPs. No such are seen close to the NP surface indicating the presence of usual for metallic NPs substantial surface structural disorder.

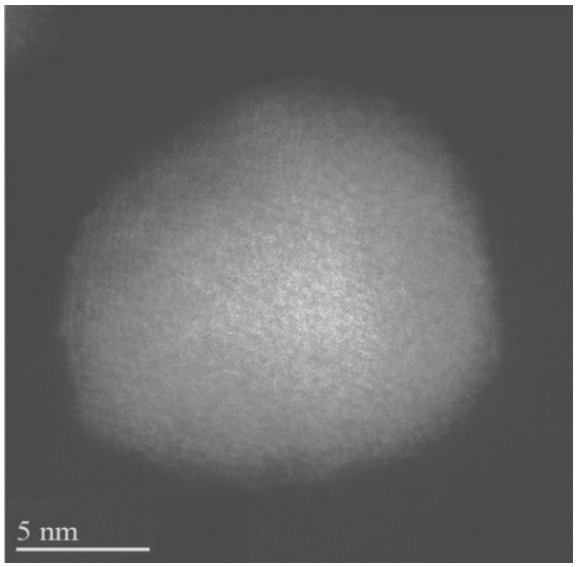

Figure S3. Representative HAADF-STEM image of ~ 16 nm in size $Fe_{48}Pd_{52}$ particle. Earlier experiments [45] have found that $Fe_{48}Pd_{52}$ NPs studied here are approximately 16(±1.5) nm in size and of alloy-type character. Both findings are in line with the HAADF-STEM image presented here.

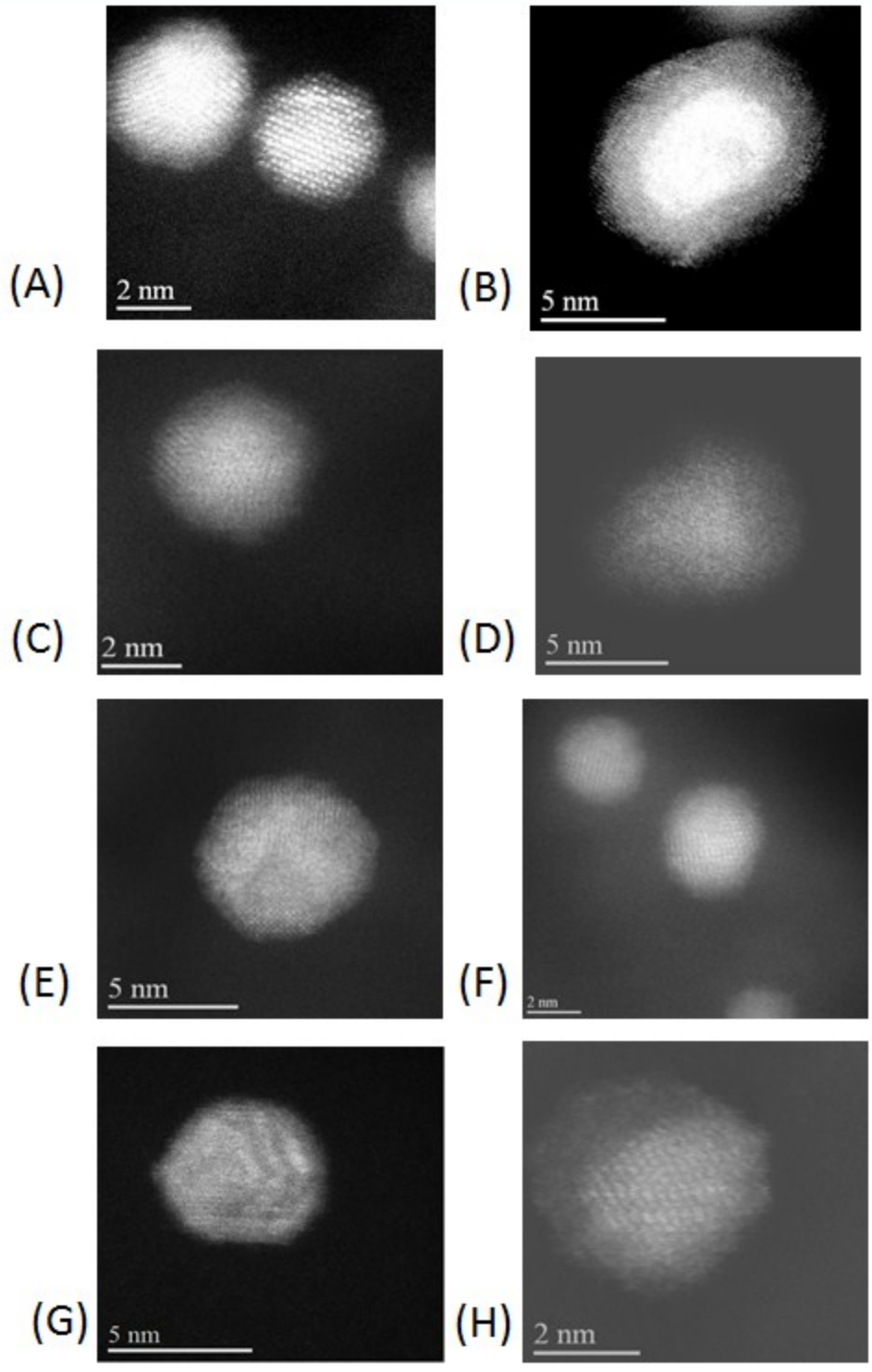

Figure S4. HAADF-STEM images of silica supported (A) fresh Au core-2 Pd layers thick shell NPs (with an overall chemical composition of $Au_{54}Pd_{46}$), (B) fresh Au core-4 Pd layers thick shell NPs (with an overall chemical composition of $Au_{42}Pd_{58}$), (C) post-synthesis treated in O_2 atmosphere alone Au core-2 Pd layers thick shell NPs as transformed into $Au_{54}Pd_{46}$ alloy NPs

and (D) post-synthesis treated in O_2 atmosphere alone Au core-4 Pd layers thick shell NPs as transformed into $Au_{42}Pd_{58}$ alloy NPs, (E) and (G) fully activated $Au_{54}Pd_{46}$ alloy NPs, (F) and (G) fully activated $Au_{42}Pd_{58}$ alloy NPs. As expected, fresh NPs (A) and (B), show clear Au core (bright area)-Pd shell (darker area) pattern with the darker area in fresh Au core-4 Pd layers thick shell NPs (B) appearing thicker than that in fresh Au core-2 Pd layers thick shell NPs (A). On the other hand, O_2 atmosphere alone treated NPs, (C) and (D), and fully activated (i.e. treated first in O_2 and then in H_2 atmosphere) NPs, (E), (F), (G) and (H), show clear Au-Pd alloy type (no sharp bright/dark contrast) pattern.

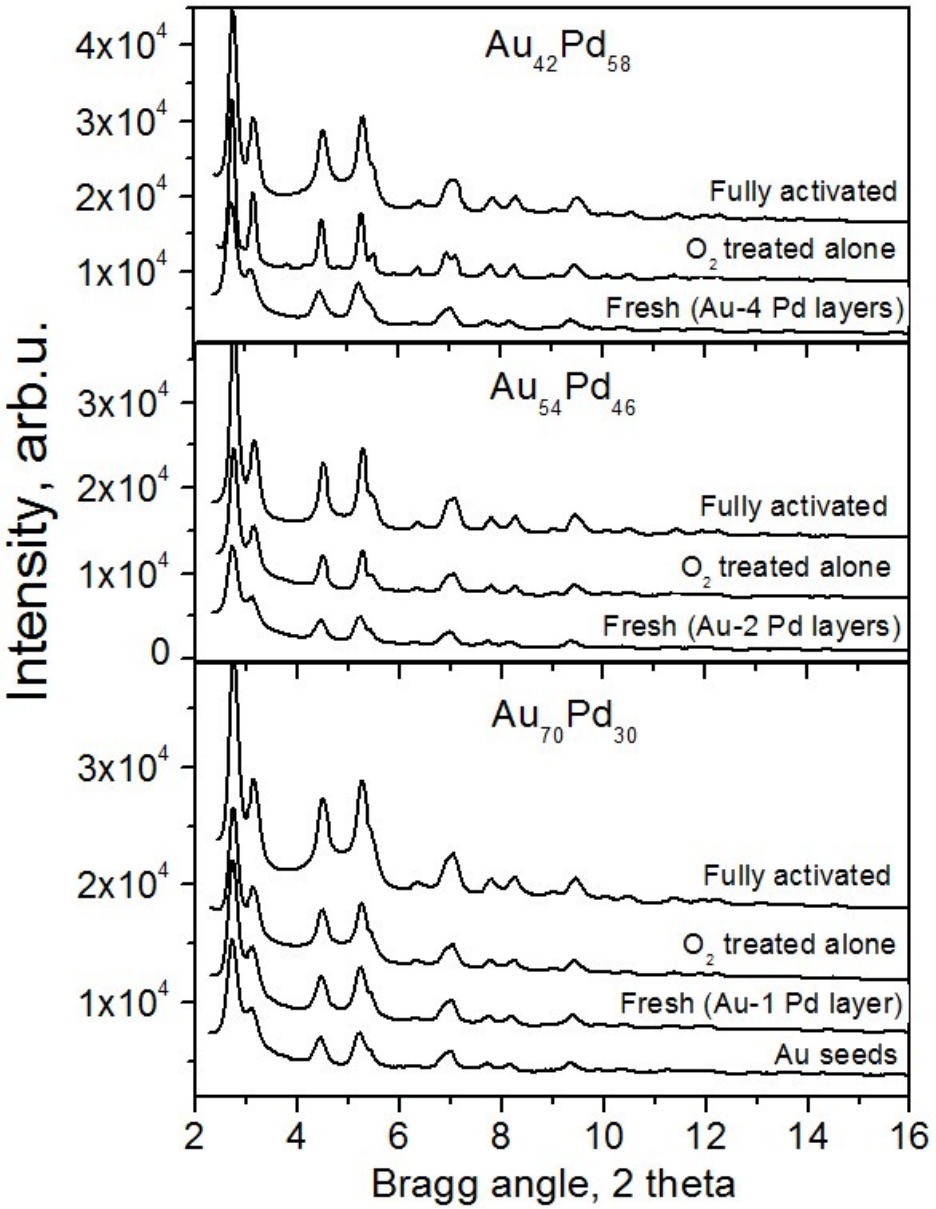

Figure S5. Background & silica support scattering corrected experimental high-energy synchrotron XRD patterns for Au seeds, fresh (Au core-Pd shell), O_2 treated alone and fully activated (O_2 + H_2 treated) $Au_{100-x}Pd_x$ NPs (x=30, 46 and 58). XRD patterns exhibit a few broad, strongly overlapping peaks at low and almost no distinct features at high diffraction (Bragg) angles, i.e. are rather diffuse in nature. Such patterns are typical for nanometer-size materials.

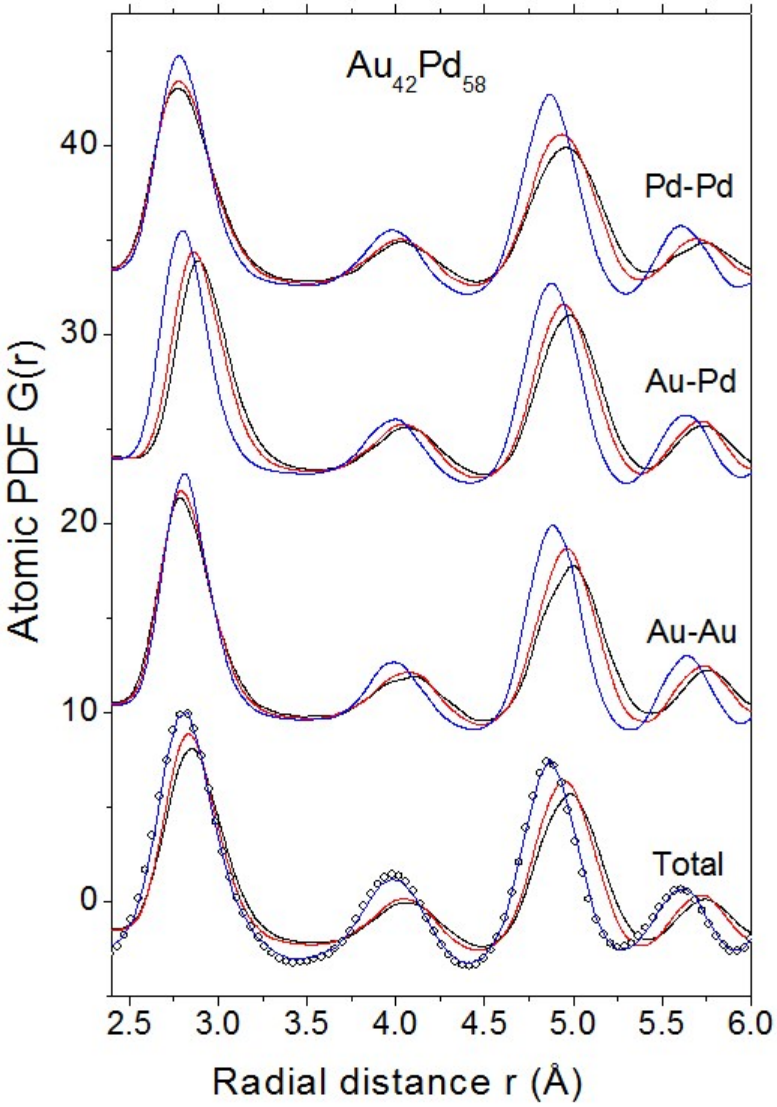

Figure S6. Total and partial atomic PDFs G(r) (full lines) for fully activated $Au_{42}Pd_{58}$ alloy NPs computed from MD models based on SC parameters a_{ii} of Table 2 and deriving Au-Pd atomic interactions (e.g. ε_{ij}) as an arithmetic ($i.e.\ \epsilon_{ij} = \frac{\epsilon_{ii} + \epsilon_{jj}}{2}$) (line in black), geometric ($i.e.\ \epsilon_{ij} = \sqrt{\epsilon_{ii}\epsilon_{jj}}$) (line in red) and harmonic ($i.e\ \epsilon_{ij} = \frac{2\epsilon_{ii}\epsilon_{jj}}{\epsilon_{ii} + \epsilon_{jj}}$) (line in blue) average of Au-Au (ε_{ii}) and Pd-Pd (ε_{jj}) interactions listed in Table 1. The experimental (total) atomic PDF for fully activated $Au_{42}Pd_{58}$ alloy NPs is also given (symbols). As data in the figure show different schemes for derivation of Au-Pd atomic interactions lead to a substantially different arrangement both of Au and Pd species in the respective models as demonstrated by the substantial differences between the partial (Pd-Pd, Au-Pd and Au-Au) atomic PDFs for the different models. As a result, the full profile of the total atomic PDFs derived from the different models, including the positions and shapes of individual PDF peaks, appears substantially different. MD model based on SC deriving

Au-Pd atomic interactions as a harmonic average of Au-Au and Pd-Pd interactions produces an atomic (total) PDF matching the experimental PDF data best.

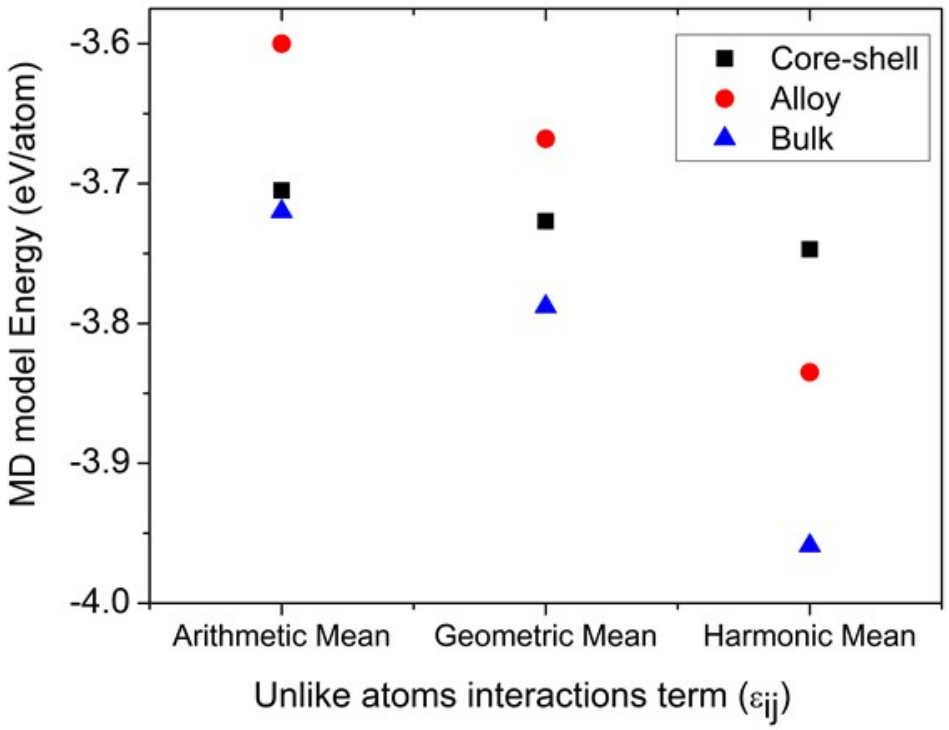

Figure S7. Energy of SC based structure models (per atom) for bulk $Au_{42}Pd_{58}$ alloy (triangles in blue), fresh Au core-4 Pd layers thick shell NPs (full squares) and obtained from them fully activated (circles in red) $Au_{42}Pd_{58}$ alloy NPs. Data are for SC models based on a_{ii} parameters of Table 2 with Au-Pd atomic interactions (e.g. ε_{ij}) derived as an arithmetic ($\epsilon_{ij} = \frac{\epsilon_{ii} + \epsilon_{jj}}{2}$), geometric ($\epsilon_{ij} = \sqrt{\epsilon_{ii}\epsilon_{jj}}$) and harmonic ($\epsilon_{ij} = \frac{2\epsilon_{ii}\epsilon_{jj}}{\epsilon_{ii} + \epsilon_{jj}}$) average of Au-Au ($\varepsilon_{ii}$) and Pd-Pd ($\varepsilon_{jj}$) interactions listed in Table 1. SC models with Au-Pd interactions derived as a harmonic average of Au-Au and Pd-Pd interactions appear lowest in energy, i.e. of highest stability.

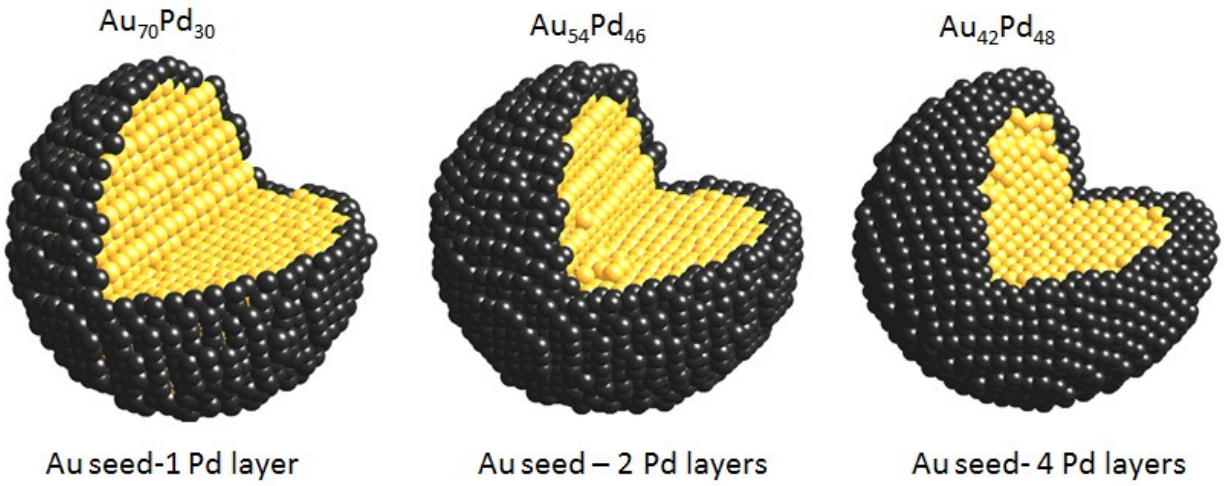

Figure S8. Real chemistry, size and shape atomic-level models for synthesized as Au core-1, 2 and 4 Pd layers thick shell NPs. The overall chemical composition of modeled NPs is also given in terms of $Au_{100-x}Pd_x$ where x=30, 46 and 58, respectively. Models are built by MD simulations based on SC method "tuned up" against experimental atomic PDFs as described in the text. Au and Pd atoms are in yellow and black, respectively.

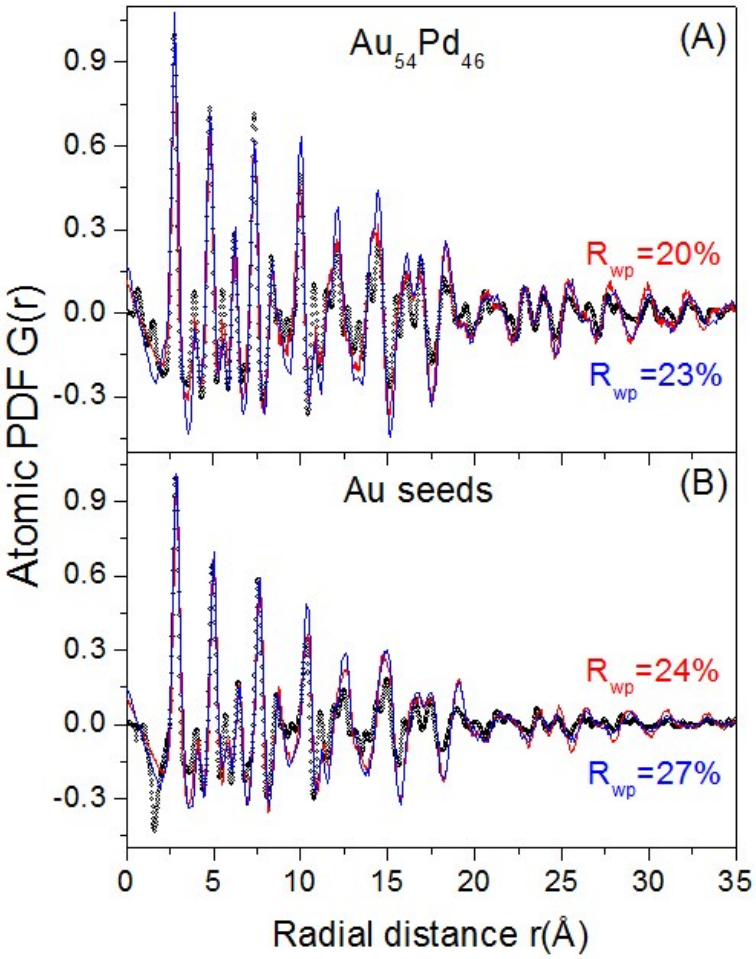

Figure S9. ***(A)*** Experimental (symbols) and model-derived (lines) atomic PDFs for fully activated $Au_{54}Pd_{46}$ alloy NPs. The PDF in red is derived from a RMC refined version (see Fig 6,right) of the MD model for $Au_{54}Pd_{46}$ alloy NPs shown in Figure 6, left. The PDF in blue is derived from an empirically disordered version of the same model. Refined values of the empirical parameters A and B (see eq. 4 in the text) are 1.01 and 0.92, respectively. ***(B)*** Experimental (symbols) and model-derived (lines) atomic PDFs for Au seeds. The PDF in red is derived from a RMC refined version (see Figure 6,right) of the MD model of Au seeds shown in Figure 6, left. The PDF in blue is derived from an empirically disordered version of the same model. Refined values of the empirical parameters A and B (see eq. 4 in the text) are 1.01 and 0.92, respectively. Model's goodness-of-fit indicators, R_{wp}, are given by each data set in color pertaining to the respective model PDF. As data in the Figure show the usually substantial atomic positional disorder in metallic NPs, manifested by the faster than expected decay of their atomic PDFs, can be incorporated in theoretical models rather accurately using an empirical or RMC-type procedures guided by experimental PDFs for the actual NPs studied. The RMC-type procedure is more accurate than the empirical one as the values of the respective R_{wp} factors show. However, as demonstrated in Figure 11, the empirical procedure put forward in this work can be extrapolated and used in theoretical prediction of metallic NPs while the RMC-type one cannot.

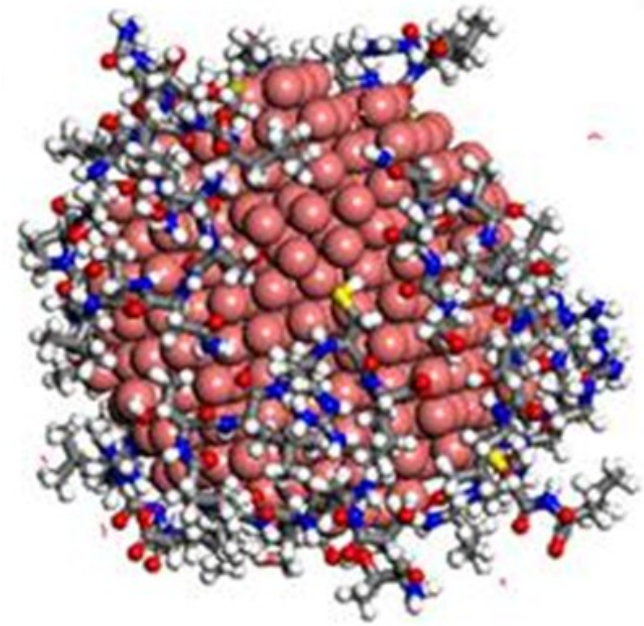

Figure S10. RMC refined 3D model of a Pd nanoparticle (in red) with atomic positional disorder accounted for precisely. Peptides, which are major building units of proteins, adsorbed on the NP surface are shown as well [78].

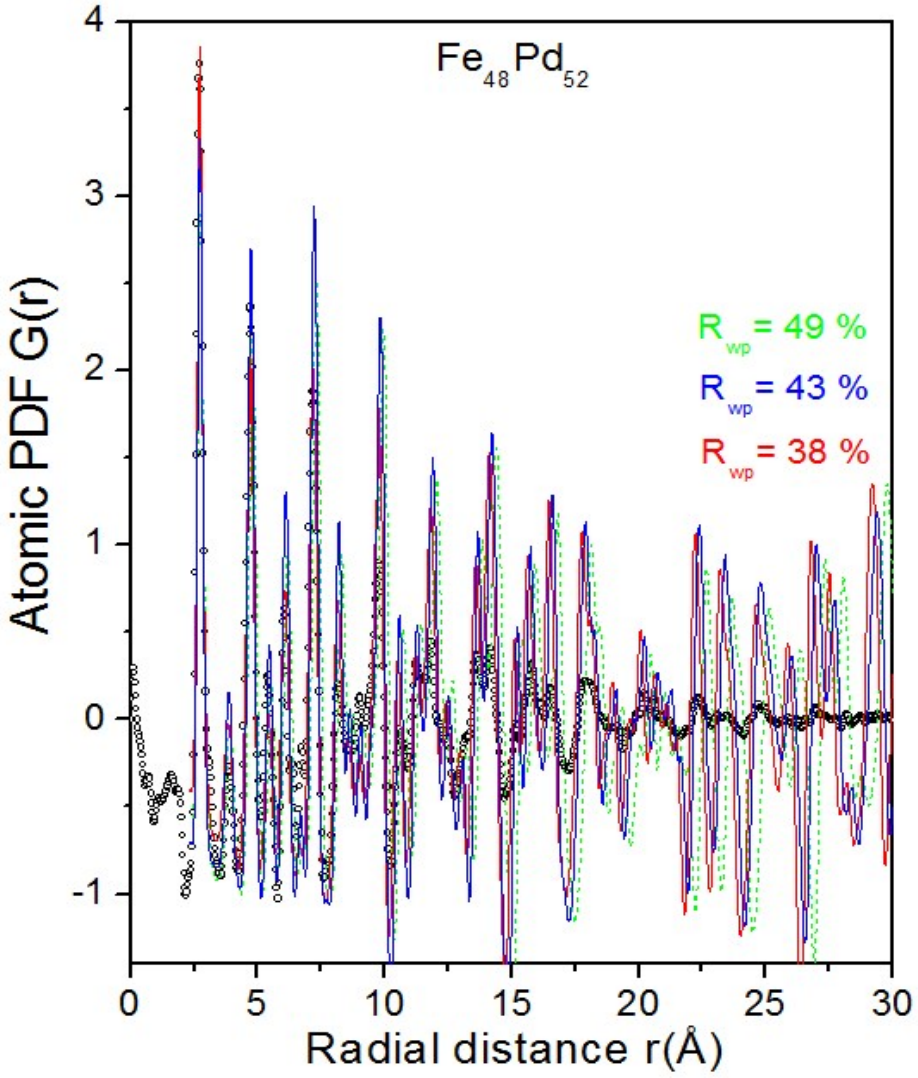

Figure S11. Experimental (symbols) and computed (lines) atomic PDFs for $Fe_{48}Pd_{52}$ alloy NPs. Computed PDFs are from MD models based on SC with Fe-Pd interactions derived as an arithmetic (line in green), geometric (line in blue) and harmonic (line in red) average of Fe-Fe and Pd-Pd interactions given in Table 3 (see text). Model's quality indicators, R_{wp}, are shown by each data set in color pertaining to the respective model PDF. As data in the Figure show models wherein Fe-Pd interactions appear as an arithmetic or geometric average of Fe-Fe and Pd-Pd interactions fail in reproducing the position and intensity of peaks in the experimental PDF data.

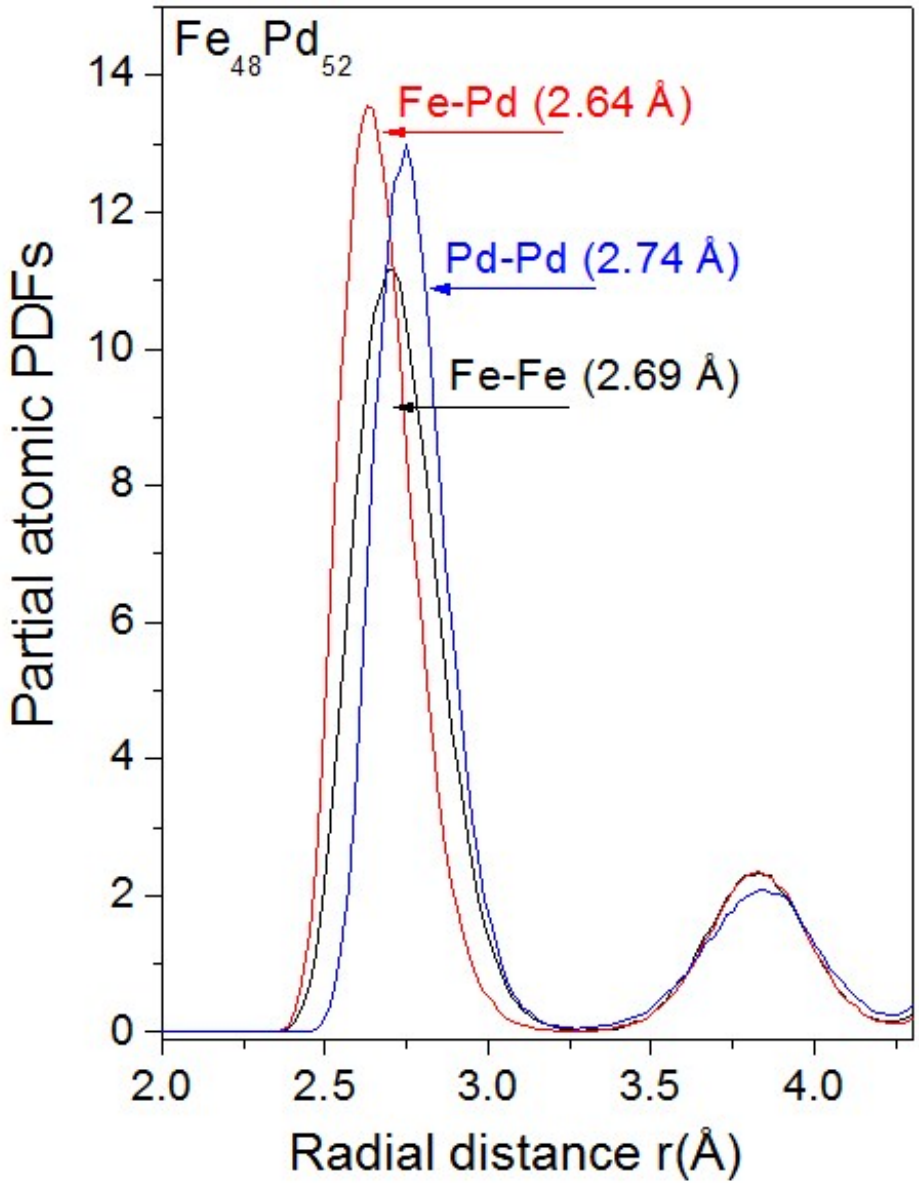

Figure S12. Partial atomic PDFs for $Fe_{48}Pd_{52}$ alloy NPs as extracted from their RMC refined 3D structure model shown in Figure 9(right). First atomic neighbor distances, as estimated from the position of the first peak in the respective partial PDF, are also given (follow the arrows).

Table S1. *Overall chemical composition of the structure models for fresh and fully activated* $Au_{100-x}Pd_x$ *NPs (x=30, 46, 58). For convenience, the composition of fresh Au core-Pd shell NPs is given both in terms of the overall number (#) of Au and Pd species and of the number (##) of Pd layers. Model's size/diameter is given as well (in nm).*

Fresh (core-shell)			Fully activated (alloy-type)		Model's size
# of Au atoms	# of Pd atoms	## Pd layers	# of Au atoms	# of Pd atoms	
2659	1146	1	2659	1146	~4.5 nm
2659	2262	2	2659	2262	~5.1 nm
2659	3704	4	2659	3704	~5.6 nm

REFERENCES:

S1. W. Smith, W. C. Yong and P. M. Rodger, "DL_POLY: Application to molecular simulation.," *Molecular Simulation,* vol. 28, p. 86, 2002.

S2. R. McGreevy and L. Pusztai, "Reverse Monte Carlo simulation: a new technique for the determination of disordered structures," *Molec. Simul.,* vol. 1, pp. 359- 367, 1998.

S3. V. Petkov and G. Junchov, "Atomic-scale structure of liquid Sn, Ge and Si by reverse Monte Carlo simulations," *J. Phys.: Condens. Matter ,* vol. 6, p. 10885, 1994.

S4. T. D. Bennett, A. L. Goodwin, M. T. Dove, D. A. Keen, M. G. Tucker, E. R. Barney, A. K. Soper, E. G. Bithell, J.-C. Tan and A. K. Cheetam, "Structure and Properties of an Amorphous Metal-Organic Framework," *Phys. Rev. Lett. ,* vol. 104, p. 115503, 2010.

S5. N. P. Funnell, M. T. Dove, A. L. Goodwin, S. Parsons and M. G. Tucker, "Local structure correlations in plastic cyclohexane-a reverse Monte Carlo study," *J. Phys.: Cond. Matter,* vol. 25, p. 454204, 2013.

S6. H. Heinz, R. Vaia, B. Farmer and R. Naik, "Accurate Simulation of Surfaces and Interfaces of Face-Centered Cubic Metals Using 12−6 and 9−6 Lennard-Jones Potentials," *J. Phys. Chem. C,* vol. 112, no. 44, pp. 17281-17290, 2008.

S7. O. Gereben and V. Petkov, "Reverse Monte Carlo study of spherical sample under non-periodic boundary conditions: the structure of Ru nanoparticles based on x-ray diffraction data," *J. Phys.: Condens. Matter,* vol. 25, p. 454211, 2013.

S8. A. Soper, "Partial structure factors from disordered materials diffraction data: An approach using empirical potential structure refinement," *Phys. Rev. B,* vol. 72, p. 104204, 2005.

S9. A. Soper, K. Page and A. Llobet, "Empirical potential structure refinement of semi-crystalline polymer systems: polytetrafluoroethylene and polychlorotrifluoroethylene," *J. Phys.:*

Condens. Matter, vol. 25, p. 454219, 2013.

S10. V. Petkov, "Nanostructure by high-energy XRD," *Mater. Today,* vol. 11, pp. 28-38, 2008.

S11. T. Egami and S. J. L. Billinge, Underneath the Bragg peaks: Structural Analysis of Complex Materials., New York: Pergamon Press, Elsevier Ltd., 2003.

S12. B. H. Toby and T. Egami, "Accuracy of pair distribution function analysis applied to crystalline and non-crystalline materials," *Acta Cryst. A,* vol. 48, p. 336, 1992.

S13. L. B. Skinner, C. Huang, D. Schlesinger, L. G. M. Petterson, A. Nillson and C. J. Benmore, "Benchmark oxygen-oxygen pair-distribution function of ambient water from x-ray diffraction measurements with a wide Q-range," *J. Chem. Phys.,* vol. 138, p. 074506, 2013.

S14. W. I. F. David, K. Shakland, L. B. McCusker and C. Baerlocher, Structure Determination form Powder diffraction., Oxford: Oxford University Press., 2002.

S15. B. H. Toby, "R factors in Rietveld analysis: How good is good enough ?," *Powder Diffraction ,* vol. 21, pp. 67-70, 2006.

S16. C. Kittel, “Introduction to Solid State Physics”, New York: John Wiley and Sons, 1976.

S17. N. M. Bedford, H.-R.-Dakhel, J. M. Slocik, B. D. Briggs, Y. Ren, A. I. Frenkel, V. Petkov, H. Heinz, R. R. Naik and M. R. Knecht “Elucidation of Peptide-Directed Palladium Surface Structure for Biologically Tunable Nanocatalysts” *ACS Nano* 9 (2015) 5082 (Journal Cover Story).